

This is an Open Access document downloaded from ORCA, Cardiff University's institutional repository: <https://orca.cardiff.ac.uk/id/eprint/130572/>

This is the author's version of a work that was submitted to / accepted for publication.

Citation for final published version:

Kopanoglu, Emre , Deniz, Cem M., Erturk, M. Arcan and Wise, Richard G. 2020. Specific absorption rate implications of within-scan patient head motion for ultra-high field MRI. *Magnetic Resonance in Medicine* 84 (5) , pp. 2724-2738. 10.1002/mrm.28276

Publishers page: <http://dx.doi.org/10.1002/mrm.28276>

Please note:

Changes made as a result of publishing processes such as copy-editing, formatting and page numbers may not be reflected in this version. For the definitive version of this publication, please refer to the published source. You are advised to consult the publisher's version if you wish to cite this paper.

This version is being made available in accordance with publisher policies. See <http://orca.cf.ac.uk/policies.html> for usage policies. Copyright and moral rights for publications made available in ORCA are retained by the copyright holders.



# Specific Absorption Rate Implications of Within-Scan Patient Head Motion for Ultra-high Field MRI

Emre Kopanoglu <sup>1</sup>, Cem M. Deniz <sup>2</sup>, Arcan Erturk <sup>3</sup>, Richard G. Wise <sup>1,4</sup>

<sup>1</sup> Cardiff University Brain Research Imaging Centre (CUBRIC), School of Psychology, Cardiff University, Cardiff, UK

<sup>2</sup> Department of Radiology, New York University, New York, USA

<sup>3</sup> Restorative Therapies Group, Medtronic, Minnesota, USA

<sup>4</sup> Institute for Advanced Biomedical Technologies, Department of Neuroscience, Imaging and Clinical Sciences, G. D'Annunzio University of Chieti-Pescara, Chieti, Italy

Running Head: Specific Absorption Rate Implications of Within-Scan Patient Head Motion for Ultra-high Field MRI

**Corresponding Author:** Emre Kopanoglu

**Address:** CUBRIC, Cardiff University, Maindy Road, Cardiff, CF24 4HQ, UK

**e-mail:** emre.kopanoglu@gmail.com

## ABSTRACT

**Purpose:** This study investigates the implications of all degrees-of-freedom of within-scan patient head motion on patient safety.

**Methods:** Electromagnetic simulations were performed by displacing/rotating a virtual body model inside an 8-channel transmit array to simulate six degrees-of-freedom of motion. Rotations of up to 20-degrees and displacements of up to 20 mm including off-axis axial/coronal translations were investigated, yielding 104 head positions. Quadrature excitation, RF shimming and multi-spoke parallel-transmit excitation pulses were designed for axial slice-selection at 7T, for seven slices across the head. Variation of whole-head SAR and 10-gram averaged local SAR of the designed pulses, as well as the change in the maximum eigenvalue (worst-case pulse) were investigated by comparing off-centre positions to the central position.

**Results:** In their respective worst-cases, patient motion increased the eigenvalue-based local SAR by 42%, whole-head SAR by 60%, and the 10-gram averaged local SAR by 210%. Local SAR was observed to be more sensitive to displacements along right-left and anterior-posterior directions than displacement in the superior-inferior direction and rotation.

**Conclusion:** This is the first study to investigate the effect of all six degrees-of-freedom of motion on safety of practical pulses. While the results agree with the literature for overlapping cases, the results demonstrate higher increases (up to 3.1-fold) in local SAR for off-axis displacement in the axial plane, which had received less attention in the literature. This increase in local SAR could potentially affect the local SAR compliance of subjects, unless realistic within-scan patient motion is taken into account during pulse design.

Keywords: ultra-high field MRI, parallel transmit, RF pulse design, patient safety, specific absorption rate, patient motion

## INTRODUCTION

Higher field strengths offer increased contrast (1) and signal-to-noise-ratio (2), which can be leveraged to produce higher image resolution (3), albeit at the cost of increased scan duration. Patient motion might become unavoidable especially with longer scans or less cooperative patients, such as in paediatric imaging (4-7), for patients with Parkinson's (8), dementia (9), or Tourette's syndrome (10). On the one hand, sedation can be used to address motion-related problems, but is unethical in research settings (10) and is invasive. Furthermore, sedation may still yield poor image quality (4), be refused by patients (9), cause adverse effects (4-6), or affect the outcomes in some applications such as functional MRI (11,12). Without sedation on the other hand, up to 13 mm translational motion and 20 degrees rotation have been reported in studies with dementia patients (13) and awake paediatric participants (14). Consequently, it is necessary to ensure the safety of the participants at UHF, in the presence of patient motion, especially for patient populations who may not stay still and may move more than healthy adult participants.

Despite the benefits of UHF-MRI, the wavelength at UHF strengths becomes comparable to body dimensions, leading to wavelength / dielectric shading /  $B_1^+$  artefacts causing contrast variations in the image. Image contrast variations are related to the excitation; therefore, contrast homogeneity cannot be recovered in post-processing and need to be corrected during scanning. Contrast homogeneity can be achieved using parallel-transmit (pTx) arrays and tailored pulses (15-20). Independent control of multiple transmit channels has raised concerns over inadvertently creating local hotspots due to constructive interference of the electric fields of different channels. Furthermore, several studies have shown that local SAR limits are reached with lower levels of input power than global SAR limits (21-23). This motivated the community to investigate the variation of local temperature and local SAR (23,24) and use those as a safety constraint in pulse design (25-29). The reader is referred to review papers for further information on RF pulse design for inhomogeneity correction at 7T (15-20).

Radiofrequency (RF) simulations allow us to characterize the three-dimensional electromagnetic field distribution in much greater detail than can be obtained via experimental measurements. Simulations involving human body models (30-32) are commonly used to obtain realistic spatial distributions of the specific absorption rate (16). Therefore, RF simulations are commonly used for safety analysis and design optimization of both pTx coil arrays and pTx pulse waveforms. The local interactions of

the fields of individual coil elements can be spatially averaged globally or locally over 1- or 10-grams of tissue and put into matrix notation. This so-called Q-matrix (33,34) can then be used to calculate local and/or global SAR for arbitrary pulses. The maximum eigenvalue of the Q-matrix provides an upper-bound on the local SAR, and it has been previously used to investigate the safety of coils (33). However, the maximum eigenvalue is often for an impractical pulse and is, therefore, over-conservative. Using the maximum eigenvalue limits pTx performance significantly, compared to local SAR calculation of practical pulses using the Q-matrices. SAR calculations can be accelerated by compressing the Q-matrices using virtual observation points (VOPs) (35). Q-matrices have been used to constrain local SAR during pulse design (29) and to calculate real-time SAR on the scanners (36).

Local SAR depends on several parameters including shape and tissue distribution of the imaged body (24,37), the type of transmit coil as well as the positioning of the body relative to the coil. Even though Q-matrices or VOPs can be used to calculate local SAR to ensure adherence to the safety limits (38,39), simulations prior to the scan may not reflect the actual scan environment accurately. Therefore, researchers have proposed using safety factors of 1.25 to account for modelling errors (40), 1.4 (24) or 1.5 (41) for inter-subject variability, 1.25 (42) or 1.55 (43) for uncertainties in the hardware, with an additional safety factor of 2 only for the eyes (42).

Patient positioning in actual scan environments may be different than that in the computational simulations used for safety calculations. These differences may be further exacerbated by patient motion, especially for patient populations who may not stay still, such as paediatric as well as Parkinson's, Huntington's, Tourette's, and dementia patients. Patient positioning influences local SAR as it affects i) loading of individual coil elements, ii) coupling of coil elements, iii) constructive/destructive interference of fields from the coil elements inside the tissue of interest, and iv) the relative position of tissues with respect to individual coil elements. Le Garrec et al. investigated the effect of displacement along anterior-posterior and superior-inferior on local SAR, suggesting a safety factor of 1.5 for RF shimming (41). Wolf et al. investigated the effect of up to 20 mm of displacement on worst-case local SAR, and reported up to 14% SAR increase (44). Shajan et al. investigated the effect of longitudinal shifts on local SAR (45) whereas Shao et al. studied longitudinal shifts as well as rotations around the three main axes (46). Murbach et al. have investigated the variation of local and global SAR with respect to patient positioning inside a birdcage body coil for displacements along the

axis of the bore for single-channel at 1.5T (47,48) and two-channel RF shimming at 3T (49,50). Deniz et al. showed that local SAR increases as coils get closer to the sample for homogeneous cylindrical and spherical objects (51). Katscher et al. showed 82% increase in overall SAR for a fixed two-dimensional Cartesian excitation trajectory when the coil array is rotated around a homogeneous spherical object (52). However, these studies focussed on different subsets of the six degrees-of-freedom of motion, and the effect of all six degrees-of-freedom of motion on local SAR has not yet been investigated for practical pulses.

This study investigates the implications of within-scan patient motion on patient safety. For this purpose, electromagnetic simulations were performed by changing the relative position of a virtual body model with respect to a generic 8-channel transmit array. All six degrees-of-freedom of motion were considered by displacing the body up to 20 mm along and rotating the body up to 20 degrees around the three Cartesian axes. Off-axis motion was also considered by displacing the body in axial and coronal planes. SAR consequences of displacements were investigated for i) quadrature excitation, ii) RF shimming and iii) multi-spoke parallel-transmit pulses that were designed for axial slice selection in head imaging at 7T. We investigated the change in i) peak local SAR, ii) the eigenvalue-based worst-case local SAR, and iii) whole-head SAR. The results showed that actual 10-gram averaged local SAR is more sensitive to motion than whole-head SAR and eigenvalue-based local SAR, and up to 210% increase in peak local SAR was observed due to patient motion, highlighting the need to consider patient motion in SAR compliance analysis.

## METHODS

Electromagnetic (EM) simulations were performed using Sim4Life (Zurich MedTech AG, Zurich, Switzerland) using the virtual body model Ella (30) for 104 different relative positions of the body model with respect to the coil structure. 43 off-centre positions were 1 mm, 2 mm, 5 mm, 10 mm, 15 mm, 20 mm towards right or inferior; 1 mm, 2 mm, 5 mm, 10 mm towards posterior;  $\pm 1^\circ$ ,  $\pm 2^\circ$ ,  $\pm 5^\circ$ ,  $10^\circ$ ,  $15^\circ$ ,  $20^\circ$  in pitch;  $1^\circ$ ,  $2^\circ$ ,  $5^\circ$ ,  $10^\circ$ ,  $15^\circ$ ,  $20^\circ$  in roll; and  $\pm 1^\circ$ ,  $\pm 2^\circ$ ,  $\pm 5^\circ$ ,  $\pm 10^\circ$ ,  $\pm 15^\circ$ ,  $\pm 20^\circ$  in yaw (Figure 1a). Values were limited in posterior and pitch to avoid an overlap between coil elements and the model. A further 60 off-axis positions were generated by changing the relative position of the model towards both right and inferior, and both right and posterior using a combination of the given shift values. The above values report the relative motion of the body model with respect to the coil structure, with positive rotation values denoting clockwise rotation around left

for pitch, anterior for roll and superior for yaw.

In EM field simulations, moving the body model may introduce two sources of error. First, changing the relative position of the model with respect to the voxelization grid may affect how tissues that are smaller than the voxel size are discretized. This may change the effective EM properties of the voxelated model, leading to inconsistencies in field calculations across different positionings. Secondly, registering the fields at different body positions to the original position requires three-dimensional interpolation. To avoid both potential sources of error, the coil structure was displaced instead.

The part of the body model inside the computation domain (Figure 1b) consisted of 47 different organs and tissues including the CSF and the shoulders as previously recommended (44). To ensure consistency across our investigations, a discretization of 2 mm isotropic resolution was enforced for the vectorized body model. The local SAR at the edge of the computation domain was verified to be always at least 30 dB lower than the spatial maximum. A generic 8-channel coil model was simulated (Figure 1b, 8 loops, 40 mm width, 110 mm height, 230 mm inner diameter, 3 mm microstrip width). Each coil element had four slots distributed around the loop; three used for 4.2 pF capacitors to tune the coil elements to the simulation frequency of 295 MHz and the fourth to model the feed port. The output resistance of the feed port was set to  $6\ \Omega$  to approximately match the average real part of the input resistance across the coil elements at the centred position. This yielded at least 10 dB return loss across all ports at the centred position. Tuning capacitor and port resistance values were kept constant across simulations. At the centred position, the minimum distance between the head and the closest coil elements was 16, 34, 17, 37 mm on the posterior, left, anterior and right sides, respectively, allowing rotations between  $-5^\circ$  and  $30^\circ$  in pitch, and between  $-30^\circ$  and  $40^\circ$  in roll. Moving the coil structure with respect to the voxelization grid can alter the properties of the loops, similar to the body model (as discussed in the previous paragraph). To minimize this effect, automatic high-resolution adaptive voxelization with 1 mm maximum voxel size was used for the coil elements. Finer voxel resolutions were also simulated for a subset of positions, which confirmed the sufficiency of the voxelization resolution used. The displacement of the coil array was executed automatically by the solver. To guard against modelling errors, coil elements were manually checked against connectivity and voxelization issues for all positions, and exported fields were verified to vary smoothly (with respect to changes in position). Because the number of voxels allocated for the coils increases for

rotations to ensure connectivity, between 6.5 million and 30 million voxels were created depending on the orientation of the coil model. The accepted input power (beyond the feed port-coil interface) in each channel was normalized to 1 W. This simulates a feedback circuitry that keeps the accepted power the same, thereby overriding imperfections in coil matching at the feed ports and any positional dependencies thereof. Coil loading and coil coupling as well as changes in these due to motion were inherently incorporated in the results. Field and tissue density data were mapped onto a predefined grid that encloses the head (size: 180x215x250 mm) and exported to Matlab (The Mathworks Inc. Natick, MA, USA), leading to consistent voxelization across all cases. Voxel-wise Q-matrices (34) were calculated using:

$$Q_{ij}(r) = \frac{1}{2\rho(r)} [J_{x,j}^H E_{x,i} + J_{y,j}^H E_{y,i} + J_{z,j}^H E_{z,i}]$$

where  $\rho(r)$  is the tissue mass density (kg/m<sup>3</sup>),  $E_{u,v}$  (V/m) and  $J_{u,v}$  (A/m<sup>2</sup>) are complex electric field and current density, respectively, along axes  $u = x, y$  or  $z$  with  $v = i$  or  $j$  being the index of the transmit channel, and the superscript  $H$  denotes Hermitian conjugation. Entries of the Q-matrix were averaged over 10-grams of tissue with cubical volumes (53). Because the three-dimensional local SAR distribution itself is of interest, virtual observation points (35) were not used in this study.

Small-tip angle pulses were designed in Matlab using an adaptation of the Matching Pursuit guided Conjugate Gradient algorithm (54) for parallel-transmit pulse design and the pulse design parameters defined for the ISMRM RF Pulse Design Challenge (55) unless specified otherwise. The cost function was defined as the sum of normalized root-mean-squared error in the excitation profile and the RF power, the latter regularized by a Tikhonov parameter,  $\lambda$  (56). An l-curve analysis was performed to characterize the trade-off between profile error and RF power for two and three spoke pulses, and consequently,  $\lambda = 0.5$  was chosen. The algorithm selected a predefined number of spokes (Ns) on a 11x11 k-space grid ( $k_x - k_y$ ) with  $\delta k_x = \delta k_y = 4 \text{ m}^{-1}$ . The  $k_x = k_y = 0$  spoke was enforced as the first spoke. During the iterations, the candidate spoke was added to the set of selected spokes, followed by the calculation of the channel-weights through minimization of the cost function using the Conjugate Gradient Descent algorithm (57). The best candidate was selected via Matching Pursuit (58). Then the channel-weights were re-optimized while relaxing the phase of the target profile (59). More detail on the algorithm can be found in (60). Time-optimal trapezoidal gradient waveforms (61) and *sinc* pulse envelopes were used for slice selection along  $z$  (62). Variable-rate selective

excitation technique was used to reduce whole-head SAR and local SAR below 3.2 W/kg and 10 W/kg, respectively (63). A total of 56 pulses were designed (28 pTx and 28 quadrature excitation) with Ns = 1 (RF shimming in the case of pTx), 2, 3 or 5 spokes for each of the seven axial slices shown in Figure 1c separately. Pulse parameters were, maximum  $B_1^+$ , 30  $\mu\text{T}$ ; maximum gradient amplitude, 40 mT/m; maximum gradient slew-rate, 140 mT/m/msec; Nc: number of coils, 8;  $\Delta t$ , dwell time, 5  $\mu\text{s}$ ; pulse time-bandwidth, 4; slice thickness, 10 mm; flip-angle, 30°; excitation field of view, 180 × 215 × 250 mm; excitation matrix size, 122 × 151 × 140; TR, 1 s; slice separation,  $\Delta z = 18 \text{ mm}$ .

Three different SAR metrics were calculated to analyse the safety effect of within-scan patient movement: (i) Local SAR refers to the three-dimensional 10-gram averaged local SAR distribution with the peak spatial value of it denoted by psSAR, (ii) hdSAR is the whole-head SAR calculated over a volume of  $4.02 \times 10^{-3} \text{ m}^3$  and a mass of 4.4 kg, (iii) eigSAR is the maximum eigenvalue of the Q-matrix. SAR results throughout the study were always normalized with their corresponding values at the head-centred position, unless specified otherwise. These SAR metrics were used to compare three different RF excitation scenarios: (i) Quadrature excitation mode combines the individual channels with equal amplitudes and progressive phases of 45-degree increments (channel weights were not optimized, 1-/2-/3-/5-spoke quadrature pulses were designed), effectively creating a single-channel volume coil, (ii) RF shimming optimizes the amplitudes and phases across each channel independently, leading to a 1-spoke pTx pulse, (iii) multi-spoke pulses optimize the amplitudes and phases independently across channels and across each spoke of 2-/3-/5-spoke pTx pulses. All pulses were designed to homogenize the in-slice excitation profile.

In order to identify the SAR implications of within-scan patient movement, RF pulses were designed using the  $B_1^+$ -maps and the Q-matrices at the centred position. Then, the peak spatial SAR of the pulse at the centred position (psSAR<sub>centre</sub>) was compared to the psSAR at the off-centre positions. Also, psSAR<sub>centre</sub> was used as a threshold for the three-dimensional local SAR distribution at the position that yields the highest psSAR increase, to characterize the size of the region that was exposed to higher local SAR than estimated initially. The volume of the region exposed to a higher level of SAR than estimated was reported in cubic centimetres. While psSAR and hdSAR are pulse/slice/position dependent, eigSAR is a value intrinsic to how the coil model and the body model are positioned with respect to each other. Hence, eigSAR yields the psSAR of the worst pulse for a position regardless of

whether that worst-case pulse is desirable in terms of its flip-angle distribution or not.

In this paper, we treat the quadrature mode as if a single-channel coil was used. This interpretation effectively changes the coil model and reduces the entries of the Q-matrix at each voxel from  $N_c \times N_c$  to  $1 \times 1$  scalars. Therefore, psSAR becomes equivalent to eigSAR, and its variation with motion becomes independent of the number of spokes and the slice position. The two metrics are equivalent only for this particular case, where the coil model was treated as a single-channel coil.

### Comparison of the three SAR metrics

Because eigenvalue-based local SAR calculations set an upper limit on local SAR, using the largest eigenvalue across all positions would ensure keeping local SAR under the limits. However, eigenvalue-based local SAR estimation is often impractically over-conservative and limits pTx performance. Further 5768 pulses (quadrature/parallel-transmit, 1-/2-/3-/5-spoke, seven slices) were designed to get a homogeneous in-slice excitation profile at each off-centre position, yielding 5824 pTx pulses in total. To compare the three SAR metrics, the duration of each pulse was adjusted such that i) its whole-head SAR was 3.2 W/kg, ii) its peak local SAR was 10 W/kg, and iii) its eigSAR was 10 W/kg, and the hdSAR and psSAR values were compared to the safety limits of 3.2 W/kg and 10 W/kg, respectively. Note that this comparison does not involve any motion or normalization with the SAR values at the centre but investigates different initial patient positions and assumes knowledge of the corresponding Q-matrix at each position.

## RESULTS

### Quadrature excitation mode

In the quadrature excitation mode, the relative weights of individual channels were fixed, making the setup akin to a single-channel volume coil such as those used in standard (non-pTx) operational modes of 7T scanners. The quadrature excitation mode is considered a much safer setup than those that allow independent control of individual channels, and guidelines recommend using whole-head SAR for supervision in this setup. Nevertheless, a region with a volume of 57 cm<sup>3</sup> was exposed to higher local SAR due to motion (Figure 2b), the location of the local hotspot changed (Figure 2a), and we observed a 2.1-fold increase in peak local SAR while the change in whole-head SAR remained below 5% (Figure 3). Note that because the relative weights of the channels are fixed the relative variation of all SAR metrics due to

motion are independent of the target imaging slice and the number of spokes for quadrature mode.

### RF-shimming

Both local SAR and whole-head SAR were observed to be more sensitive to motion for RF shimming than the quadrature mode. The worst case was observed for RF shimming in mid-brain, in which case the local hotspot moved from the left temple to the right-posterior part of the head (Figure 4a), and a region with a volume of 79 cm<sup>3</sup> was exposed to higher local SAR (Figure 4b). While eigSAR and hdSAR increased by up to 42% and 33% (data not shown) in their respective worst-cases, respectively, and by 42% and 10% for the case in Figures 4-5, the peak local SAR increased by up to 2.4-fold (Figure 5). For RF shimming, seven pulses were designed, with peak local SAR increasing by more than 50% in all cases and the increase being more than 100% for five pulses. The worst-cases for eigSAR and hdSAR were different than that of psSAR. This shows that the sensitivity of each parameter to patient motion is different, highlighting that peak local SAR (psSAR) cannot be substituted by the others.

### Multi-spoke pulse design

Multi-spoke pulses were more sensitive to patient motion than RF shimming and quadrature excitation. Figure 6 compares the local SAR distribution after motion to the maximum local SAR before motion (psSAR) for 2-spoke, 3-spoke and 5-spoke pulses. The largest region exposed to higher local SAR was for the 5-spoke pulse with a volume of 263 cm<sup>3</sup>, whereas the highest increase in peak local SAR was for the 3-spoke pulse, in which case the peak local SAR increased by 3.1-fold (Figure 7).

Because eigSAR compares the worst pulses for each location, the estimated SAR increase for the multi-spoke pulses was the same as the RF shimming case (Figure 5), and therefore, it was omitted. While the whole-head SAR and peak local SAR showed similar variations (Figure 7, Supporting Information Figures S2 and S3), the change in whole-head SAR underestimated the increase in peak local SAR, as whole-head SAR increased by up to 60%, 60%, and 18%, whereas the peak local SAR increased by up to 2.6-fold, 3.1-fold, and 2.2-fold for the 2-, 3- and 5-spoke pulses, respectively. Across the 21 multi-spoke pTx pulses peak local SAR increased by 50% or more for 13 pulses (62%), by more than 100% for 5 pulses (24%), and by more than 150% for 3 pulses (14%).

The local SAR increased mainly in the regions that get closer to the coils as expected. However, this is not a trivial dependence on coil-to-tissue distance, as it depends on the relative power applied

through each channel and the corresponding interference of the electric fields of the channels. This is highlighted by the differences between the worst-case displacement scenarios (R: 20 mm for the 2-spoke pulse vs R: 20 mm & P: 10 mm for the 3-spoke and 5-spoke pulses, Supporting Information Figure S1) and the location, size and shape of the regions exposed to increased local SAR. Furthermore, the maximum increase in psSAR was not observed for the head position with minimum distance between the tissue and the nearest coil element for the 2-spoke pulse, supporting the notion that the change in local SAR depends on channel weights rather than just the coil-to-tissue distance.

Comparing the SAR metrics for all 28 pTx pulses showed that whole-head SAR substantially underestimated the variation in peak local SAR (Figure 8). While rotational motion led to less than 40% variation in psSAR for all pulses, psSAR more than doubled for several motion types and pulses. EigSAR variation is the same as shown in Figure 5, and hence, omitted in this figure.

The variation in peak local SAR due to motion was more extreme than hdSAR and eigSAR. The SAR metrics for all 28 pulses were normalized by their respective values at the centred position and sorted in decreasing order with respect to psSAR (Figure 9a). The eigenvalue approach yielded a maximum increase of 42%, which is similar to previous literature (41), while hdSAR yielded a higher maximum increase of 60%. Both eigSAR and hdSAR underestimated the increase in peak local SAR, which increased by up to 3.1-fold. Furthermore, eigSAR does not provide information about the actual pulse and the variation of eigSAR is substantially different than that of psSAR. In fact, for some cases where psSAR more than doubled, eigSAR estimated around 10% increase (magnified inset, panel a). Although hdSAR showed a similar overall variation to psSAR, the metrics are not always consistent. As an example, for two cases in which hdSAR increased by approximately 10%, psSAR doubled on one and decreased by 10% in the other.

PsSAR also showed larger reductions (39%) compared to hdSAR (Figure 9a), even at positions where hdSAR increased. For 40% of the off-centre positions investigated, the relative change in hdSAR was up to 43% higher than the change in psSAR compared to the values at the centre, while the relative change in peak local SAR was up to 121% higher for 60% of the positions (Figure 9b). Even though setting psSAR equal to 10 W/kg at the centre led to hdSAR exceeding 3.2 W/kg by less than 6% for both quadrature and parallel-transmit (Figures 9c-d), this overshoot depends on the coil model.

When hdSAR was set to 3.2 W/kg at the centre, psSAR exceeded 10 W/kg in 73% of the cases with quadrature excitation and almost all pTx cases. Peak local SAR values of up to 21 W/kg and 81 W/kg were observed for quadrature and parallel-transmit (Figures 9e-f). When psSAR at the centre was set to 10 W/kg, psSAR at other positions exceeded the limit in 64% and 62% of the cases, yielding as high as 31 W/kg for parallel-transmit.

### Comparison of the three SAR metrics

The SAR metrics were compared for a total of 5824 pulses designed for each setup, each slice and each positioning. When hdSAR was used as the sole safety metric and set to 3.2 W/kg in the head at each position, local SAR was observed to be as high as 20.4 W/kg and 41 W/kg, exceeding the limit in normal operation mode in 86% and 99.5% of the cases for quadrature and parallel-transmit, respectively (Figure 10b). HdSAR exceeded 3.2 W/kg by up to 8% in less than 15% of the cases for quadrature, and in a minority of the cases for parallel-transmit (Figure 10a) when psSAR was set to 10 W/kg. EigSAR overestimated SAR compared to both metrics; when eigSAR was used as the safety metric, hdSAR was at or below approximately 12% of its limit, and psSAR was overestimated by between 2.6-fold and 17.1-fold for parallel-transmit (Figure 10d). On average, eigSAR overestimated psSAR by 6.9-fold, and hdSAR underestimated psSAR by 1.8-fold.

## DISCUSSION

The aim of this study was to investigate the effect of within-scan patient motion on SAR-related patient safety at ultra-high field. A virtual body model was simulated at 104 relative positions inside an 8-channel transmit array. Quadrature excitation, RF shimming, and multi-spoke pTx pulses were designed for axial slice-selection for seven different slices throughout the brain. Up to 3.1-fold increase was observed in 10-gram averaged peak local SAR due to patient motion, and the peak local SAR increased by more than 100% for one-third of the designed pulses. Peak local SAR was observed to be more sensitive to displacement in the axial plane than displacement along superior-inferior direction and rotation of the head.

Single-channel volume coils are generally assumed to be much safer than parallel-transmit due to the limited degrees of freedom, and guidelines prescribe whole-head SAR control rather than local SAR. Here, we investigated the quadrature excitation mode, which essentially makes the parallel-transmit coil similar to a single-channel coil. In this case, the results demonstrated a 2.1-fold increase in peak local SAR and up to 21 W/kg peak local SAR for the coil model used.



The sensitivity of peak local SAR to patient motion increased as more degrees of freedom were introduced into pulse design, with RF shimming being more sensitive than quadrature and multi-spoke pTx pulses being the most sensitive to patient motion. However, the sensitivity of SAR to patient motion did not increase with the number of spokes of a multi-spoke pulse. There are two potential reasons for the non-monotonic change of sensitivity to motion with the number of spokes. First, the pulse optimization method re-optimizes the channel weights for the previously selected spokes when a new spoke location is selected. Therefore, while the first two spokes of a 3-spoke pulse are the same as a 2-spoke pulse for the same slice, the channel weights are different. Second, the changes due to motion reported in this paper are relative rather than the absolute local SAR values. Thus, even without re-optimization of the channel weights, the last spoke might be individually less sensitive to patient motion than the preceding spokes, leading to a less pronounced overall relative change with respect to the centred position than a pulse with a lower number of spokes. SAR variations were investigated for pulses designed for seven slices across the brain, but no specific brain region could be identified, for which the SAR of the designed pulses are more sensitive to patient motion.

For parallel-transmit, peak local SAR was observed to be more sensitive to patient motion than eigenvalue based worst-case SAR estimates (eigSAR) and whole-head SAR. Eigenvalue-based SAR estimates are independent of the number of spokes and the target slice, and do not provide practical information about the actual pulse. Furthermore, the location of the volume of tissue with eigSAR may be completely different from the location where the peak local SAR is observed. Therefore, the pattern of variation of eigSAR was significantly different than those of whole-head SAR and peak local SAR. Because eigSAR finds the upper limit of local SAR for each position of the body model, using eigSAR with an appropriate safety margin for motion would ensure the local SAR compliance of all pulses designed here. However, eigSAR can be significantly over-conservative, which will hamper the performance of parallel-transmit systems. EigSAR was compared to the actual peak local SAR (psSAR) for 2912 pTx pulses, yielding between 2.6-fold and 17.1-fold overestimation. On the average, eigSAR overestimated psSAR by 6.9-fold. Hence, using online local SAR supervision with amplitude and phase information instead of the eigenvalue approach makes it possible to better utilize the benefits and the flexibility of the pTx systems. However, the discrepancies between the computational model and the subject including the effect of patient position becomes more important, as peak local

SAR was observed to be more susceptible to patient motion than eigSAR.

Whole-head SAR generally followed similar patterns of variation with the peak local SAR, although the maximum increase observed was much lower at 60%, as opposed to the 210% increase in peak local SAR. The difference in values, and dissimilarities in variation are due to the integration of the deposited power over the whole head for hdSAR. Even though the regions that were exposed to increased levels of local SAR were on the order of a couple of hundred cubic centimetres for various cases, the drop in local SAR in the rest of the head mitigated the increase in whole-head SAR, leading to dissimilarities between the two safety parameters. As an example, for two cases in which whole-head SAR increased by approximately 10%, peak local SAR increased by 100% in one case and decreased by 10% in the other.

The accepted power in each channel was normalized to 1 W in this study, overriding the reflections at the interface between the feed port and the coil for coil feeding purposes. This effectively simulates a feedback system that maintains the accepted power across cases and coils. However, not all the power is delivered to the body model as it is partially radiated, dissipated in the lumped elements of the coil element, or dissipated in the lumped elements and sources of the coupled coil elements. The reflections at the coil-port interface due to imperfect matching were included in coil coupling calculations. Coil matching and tuning were performed only at the centred position and the effect of positional variations on coil loading, coil matching and tuning, and coil coupling were inherently incorporated in the results (except for the scaling of the accepted power that partly overrides the effects of coil matching). These variations affect the electromagnetic field distributions, and consequently, local SAR. Furthermore, the ratio of the power that was delivered to the body to the total accepted power changes, leading to variations in whole-head SAR. Other coil designs such as shielded coils, overlapping loops, microstrip coils, and antenna elements may behave differently. Having a feedback system that maintains the accepted power regardless of positional variations may not necessarily be realistic. To investigate the effect of this normalization, the power delivered to each coil before normalization was investigated for the centre position and the position with maximum translation in the axial plane, and was observed to vary by less than  $\pm 8\%$  across simulations, which is relatively minor compared to the 60% increase in whole-head SAR and 210% increase in peak local SAR.

In addition to whole-body SAR supervision, safety guidelines recommend whole-head and local SAR supervision for volume and local transmit coils, respectively, and specifying appropriate SAR



control for pTx depending on usage as pTx coils have attributes of both types of coils (64). Even though psSAR showed more extreme increases due to motion than hdSAR, one metric cannot necessarily be substituted by the other due to the dissimilarity between the metrics. In the cases where motion was simulated, psSAR exceeded 10 W/kg by up to 2.1-fold (quadrature) and 8.1-fold (pTx) when hdSAR was used as the sole safety metric, and psSAR increased more rapidly than hdSAR in 60% of the cases. However, hdSAR either increased more rapidly or decreased less rapidly than psSAR in 40% of the cases. In the case without motion, where pulses were designed for and evaluated at each position, psSAR and hdSAR both exceeded their respective limits, when the other metric was used as the sole safety metric. While across both cases (with and without motion) hdSAR exceeded 3.2 W/kg less often than psSAR exceeded 10 W/kg, this is partly due to the coil model used here. For a coil that yields lower peak local SAR for the same level of hdSAR, this dissimilarity between motion sensitivity of the metrics could lead to hdSAR exceeding 3.2 W/kg more if peak local SAR is used as the sole safety metric. These comparisons of the SAR metrics here showed that neither whole-head SAR, nor peak local SAR were consistently more conservative than the other, highlighting the necessity of using both metrics in pulse design.

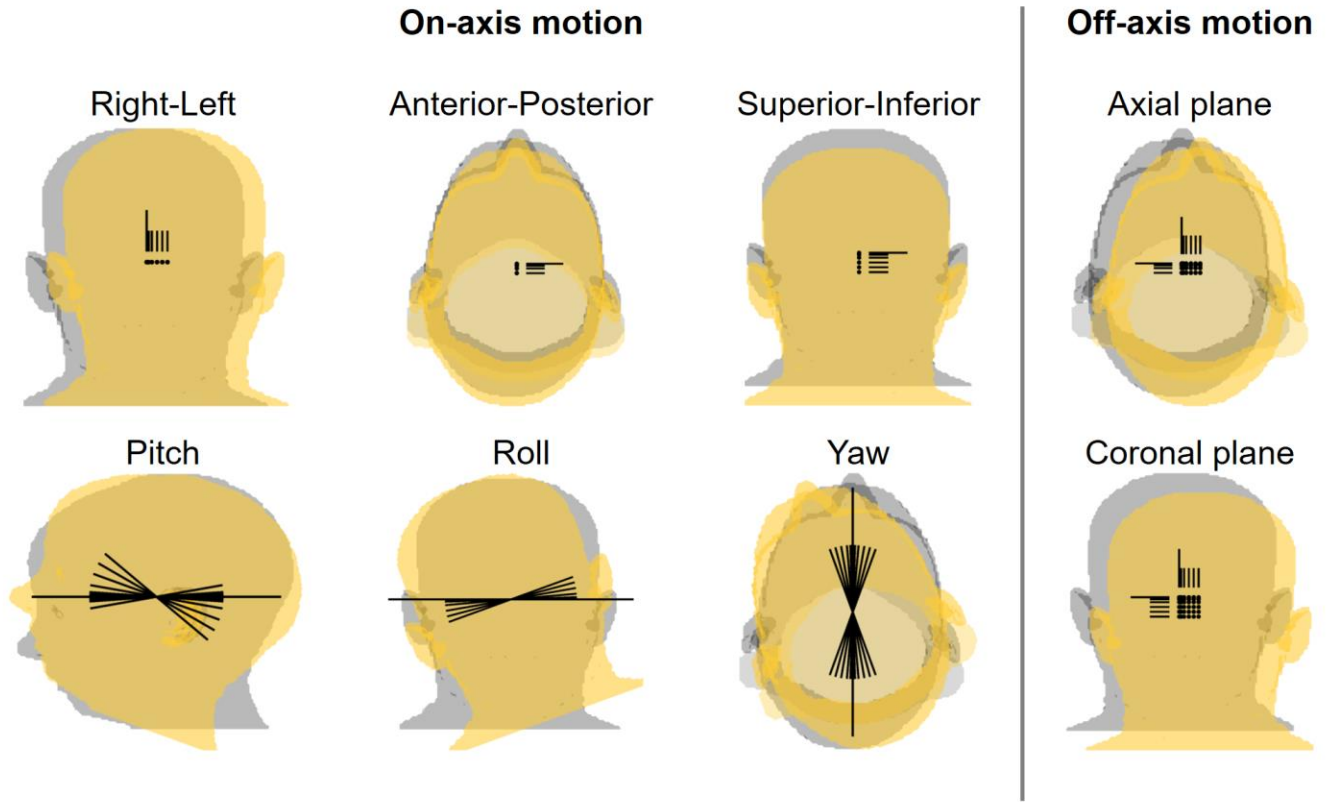
In the literature, Le Garrec et al. conducted a probabilistic analysis of local SAR variations and reported that a safety margin of 1.5 is unlikely to be exceeded (41). However, only translations along anterior-posterior and superior-inferior were considered out of all six degrees-of-freedom of motion. Here, our results for translation along those two directions are in agreement with (41). Nevertheless, we observed the largest increases in local SAR for simultaneous motion along both anterior-posterior and right-left, plausibly because these types of motion move the body closest to the coil elements. Wolf et al. investigated the effect of up to 20 mm of displacement on eigSAR and reported up to 14% increase (65). Here, we have observed up to 42% variation in eigSAR. The differences may be attributed to differences in computational models used. Murbach et al. have investigated the variation of local and global SAR with respect to patient positioning inside a birdcage body coil for displacements along the axis of the bore for single-channel at 1.5T (47,48) and two-channel RF shimming at 3T (49,50). The variations in SAR in these studies were more extreme compared to our results as the effect of imaging different parts of the body rather than patient motion was investigated. Boulant et al. reported less than 10% variation in local SAR due to longitudinal shifts, which is in agreement with our results as we observed that

local SAR was less sensitive to shifts in superior-inferior direction than anterior-posterior and right-left (45).

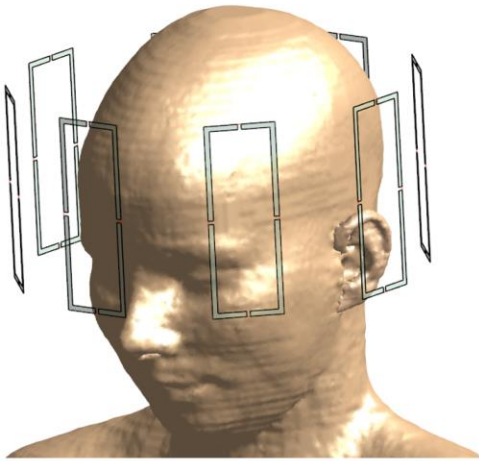
Here, we showed that a within-scan positional variation could cause a 3.1-fold increase in peak local SAR. This increase was observed for a realistic pulse designed for homogeneous slice-selection rather than an impractical worst-case pulse. The peak local SAR variations reported here relate to when the patient position changes during the scan, and do not take other computational-experimental mismatches into account. An important such mismatch is a difference in initial patient positioning in the computational models used for safety calculations and the actual scan. The effect of a potential underestimation due to this mismatch could further exacerbate the peak local SAR variations reported here. Therefore, we propose that the effect of positional uncertainty on local SAR should be investigated in more detail, especially when creating online safety supervision tools/models for coils.

Our study has limitations. All 6 degrees-of-freedom of motion were investigated, as well as off-axis motion in axial and coronal planes, yielding a dataset with 104 positions in total. However, the rotations were around the centre of the coil rather than a pivot point in the neck and the head was translated in the posterior direction rather than anterior, potentially rendering these cases unrealistic for patients lying in supine position. Furthermore, the dataset is far from being comprehensive as other combinations of degrees-of-freedom of motion were not investigated here, and nor were other body models. The simulations were conducted for a generic coil model and therefore, the 3.1-fold peak local SAR increase observed in this study should not be used as a local SAR compliance margin for a different coil. Nevertheless, we believe that more comprehensive simulations are required to ensure local SAR compliance of parallel transmit coils and pulses. In practice, scanners use VOPs for online local SAR supervision to determine the local SAR compliance of a sequence. However, due to the extensive resources required for the simulations, a limited number of body models / positions are used for creating the VOPs. Nevertheless, to ensure local SAR compliance of a sequence in the presence of motion, VOPs that incorporate multiple body models simulated at multiple locations are highly likely to be required for online supervision, in addition to clearer communication of the cases considered in these simulations to the end-users. Efforts towards SAR compliance can also be improved by incorporating simulations at multiple locations for a limited but more realistic range of body motion with an automatic scan shutdown if excess motion is detected.

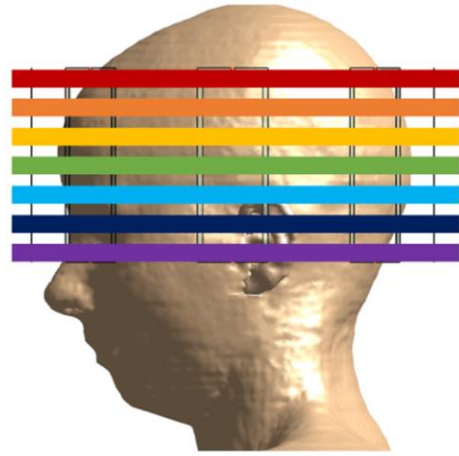
# FIGURES



(a)



(b)



(c)

Figure 1: **(a)** All six degrees-of-freedom of motion and two off-axis displacements were studied. Images indicate how the body model moves relative to the coil. Grey and yellow shaded head models represent the original position and the farthest off-centre position, respectively. Markers and lines indicate the centre of the body model for cases with displacement and the central axis of the body model for cases with rotation. Longer lines indicate the case without motion. **(b)** Relative position of the body model with respect to the coil elements in the central position is shown. The shoulders were included in the simulations but excluded in the view here. **(c)** Pulses were designed for the presented seven axial slices. Slice thicknesses are not to scale.

## Quadrature excitation

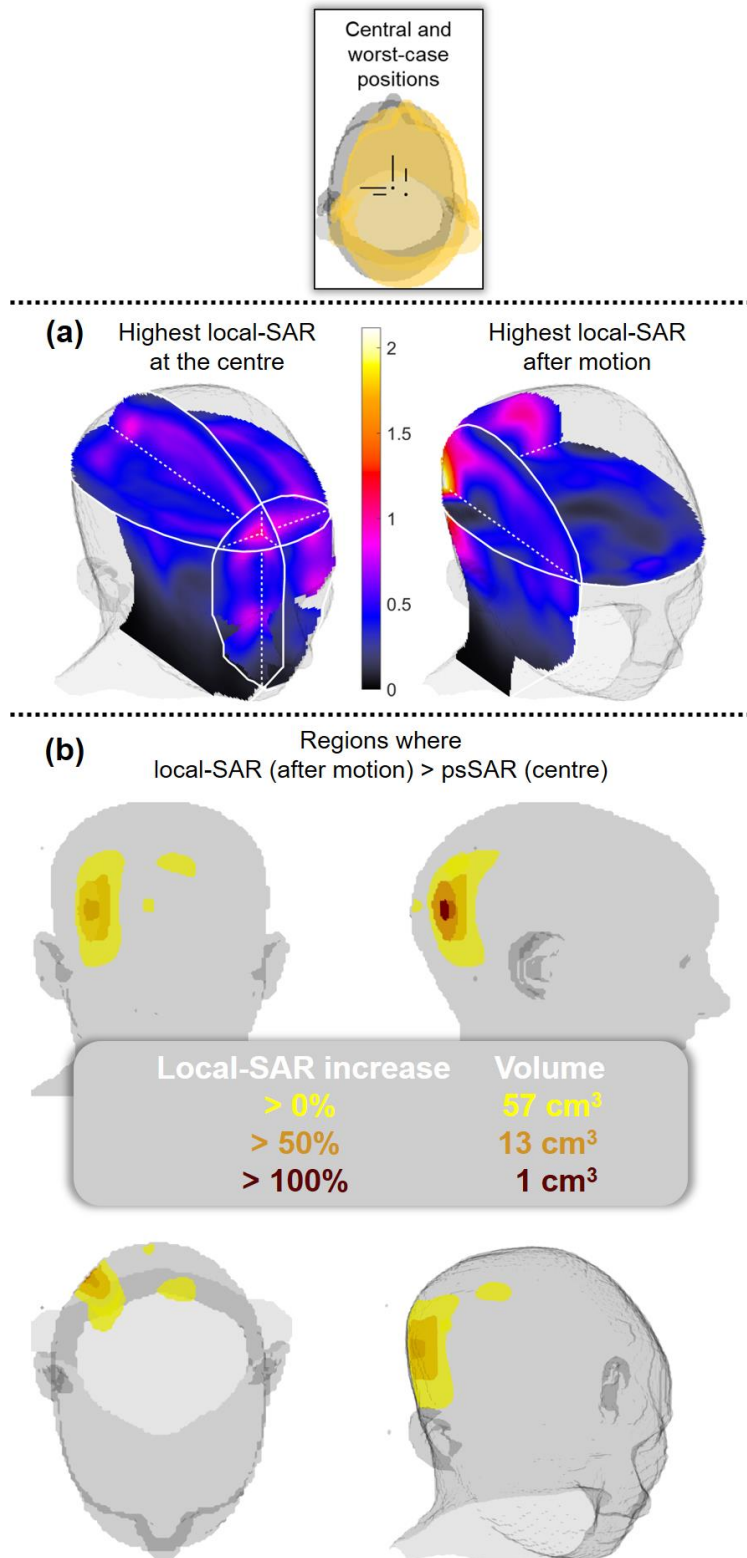


Figure 2: Three-dimensional comparisons show how local SAR changes with patient motion in the quadrature excitation mode. The worst-case increase was observed for R: 20 mm, P: 10 mm motion as indicated in the inset in the top row. **(a)** The local hotspot (intersection of the three planes) moved from the anterior to the posterior part of the brain. **(b)** The highlighted regions demonstrate where local SAR after motion exceeded the estimated peak local SAR ( $\text{psSAR}_{\text{centre}}$ ) at the centred position, more than doubling in the red-shaded region. The demonstrated changes are independent of the slice position and the number of spokes.

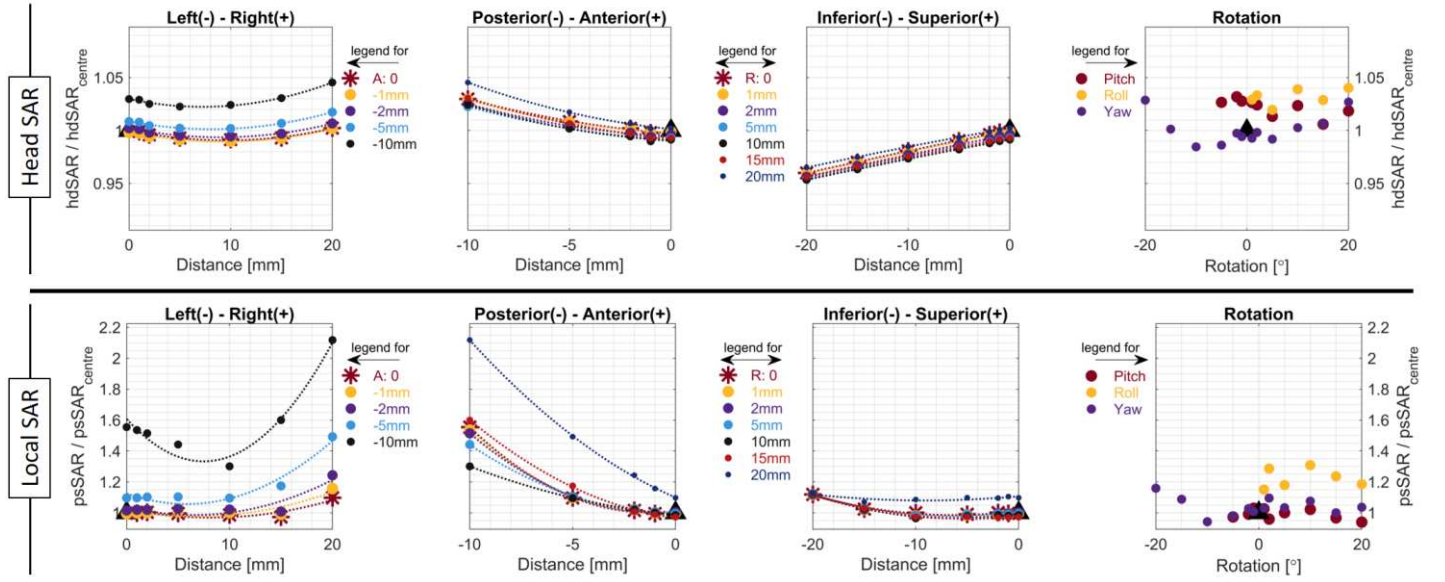


Figure 3: The variation of psSAR and hdSAR due to patient motion when the coil is used in the quadrature excitation mode. Because the coil was treated as a single-channel coil in the quadrature excitation mode, psSAR is equivalent to eigSAR and the variation of all three SAR metrics due to motion is independent of target slice and number of spokes. While the variation in whole-head SAR was below 5%, psSAR increased by up to 2.1-fold in the quadrature excitation mode due to patient motion.

## RF shimming

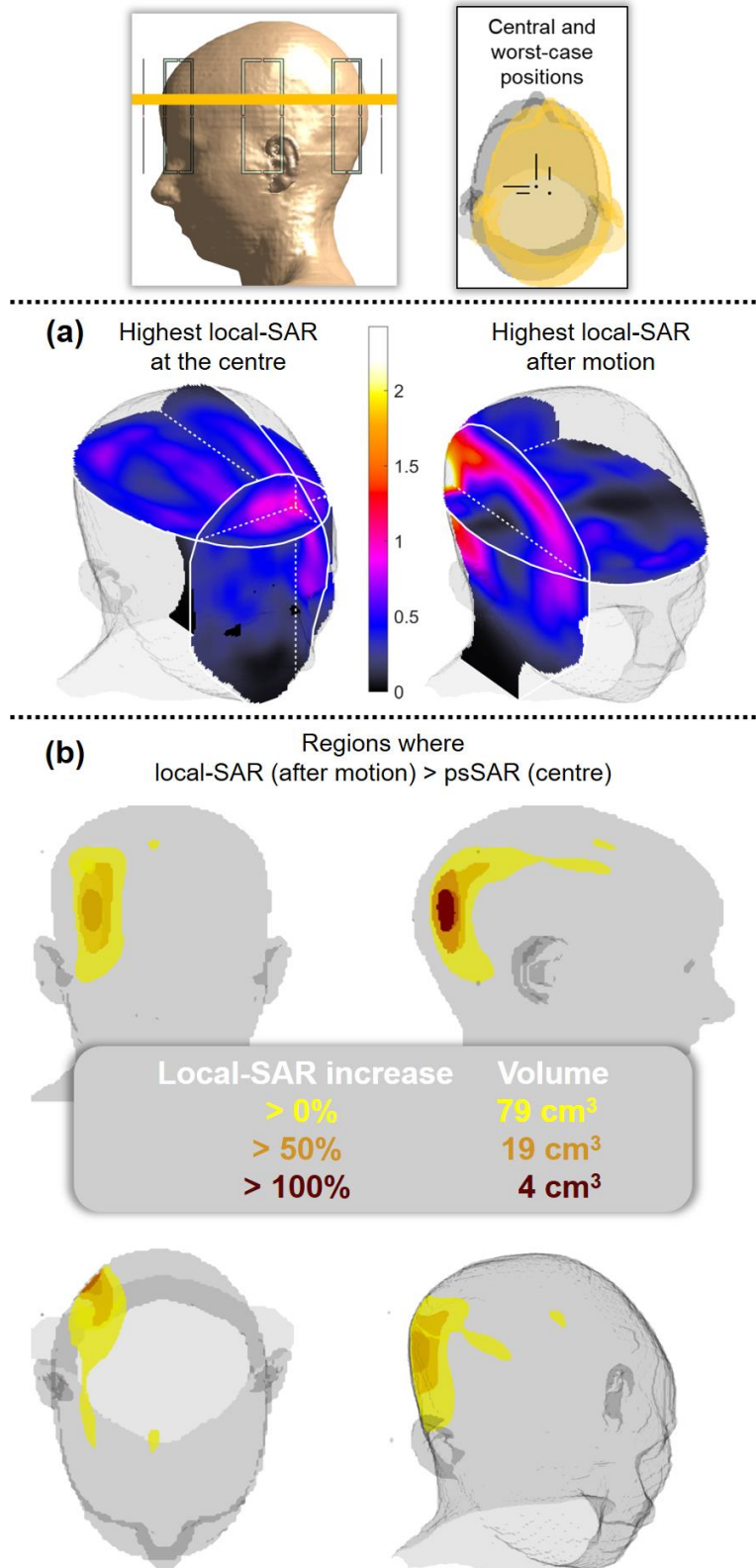


Figure 4: Three-dimensional comparisons show how local SAR changes with patient motion for RF shimming. The worst-case increase was observed for R: 20 mm, P: 10 mm motion as indicated in the inset. The highlighted regions demonstrate where local SAR exceeded the estimated peak local SAR (psSAR) at the centred position. Peak local SAR increased by 2.4-fold due to motion.



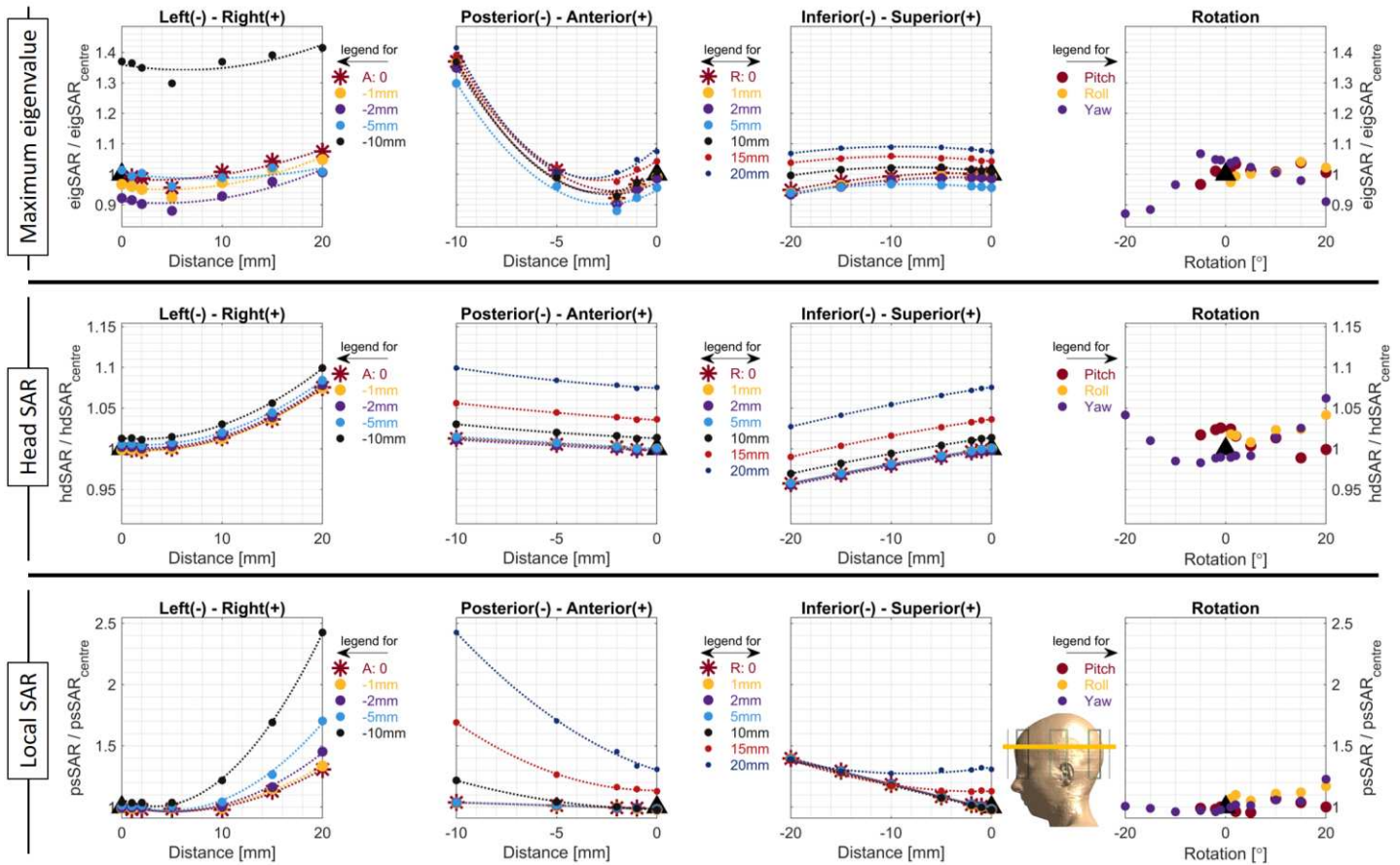


Figure 5: The variation of psSAR, eigSAR and hdSAR due to patient motion when the coil is used for RF shimming (slice of interest shown as an inset in the bottom right panel). EigSAR yielded an increase of up to 42%. For the RF shimming weights designed for the depicted slice, hdSAR increased by up to 10%. However, the actual peak local SAR (psSAR) increased by up to 2.4-fold due to patient motion for RF shimming.

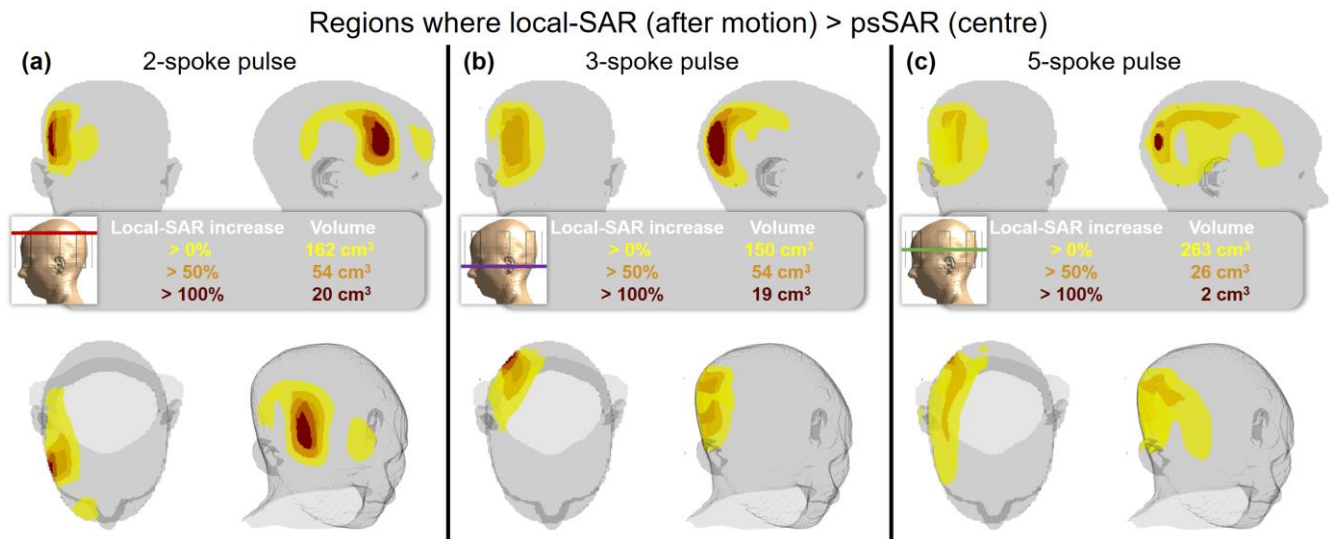


Figure 6: Three-dimensional comparisons show how local SAR changes with patient motion for three multi-spoke pulses. The worst-case increase was observed for R: 20 mm displacement for the 2-spoke pulse and R: 20 mm, P: 10 mm displacement for the 3-spoke and 5-spoke pulses. The highlighted regions demonstrate where local SAR exceeded the estimated peak local SAR at the centred position (psSAR). For the 2-spoke pulse, the local hotspot was in the right-anterior part of the brain whereas for the 3-spoke and 5-spoke pulses, it was in the right-posterior part. The local hotspots did not change position for the three pulses shown here due to motion (local hotspots shown in Supporting Information), although the peak local SAR increased **(a)** 2.6-fold for the 2-spoke pulse, **(b)** 3.1-fold for the 3-spoke pulse, and **(c)** 2.2-fold for the 5-spoke pulse.

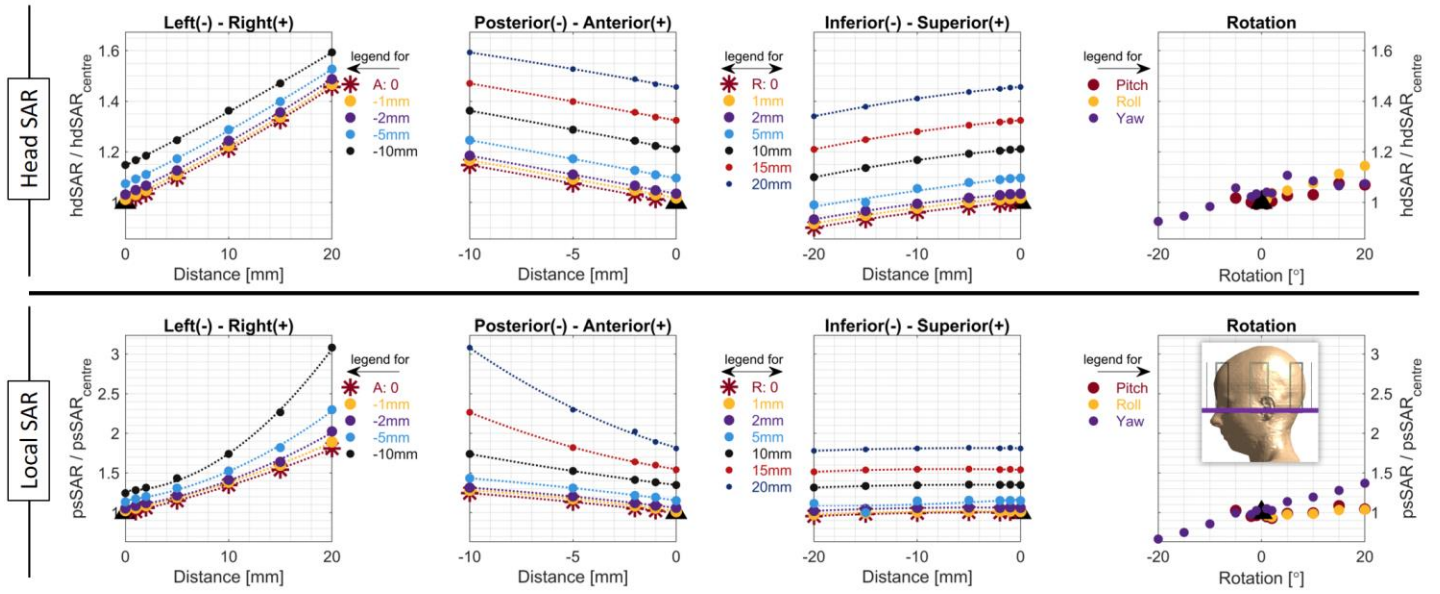


Figure 7: The variation of whole-head and peak local SAR due to patient motion for a 3-spoke pulse (target slice shown on bottom right). EigSAR (same as in Figure 5), yielded a maximum increase of 42% whereas hdSAR increased by up to 60%. However, both metrics underestimated the actual increase in peak local SAR (psSAR), which increased by up to 3.1-fold.

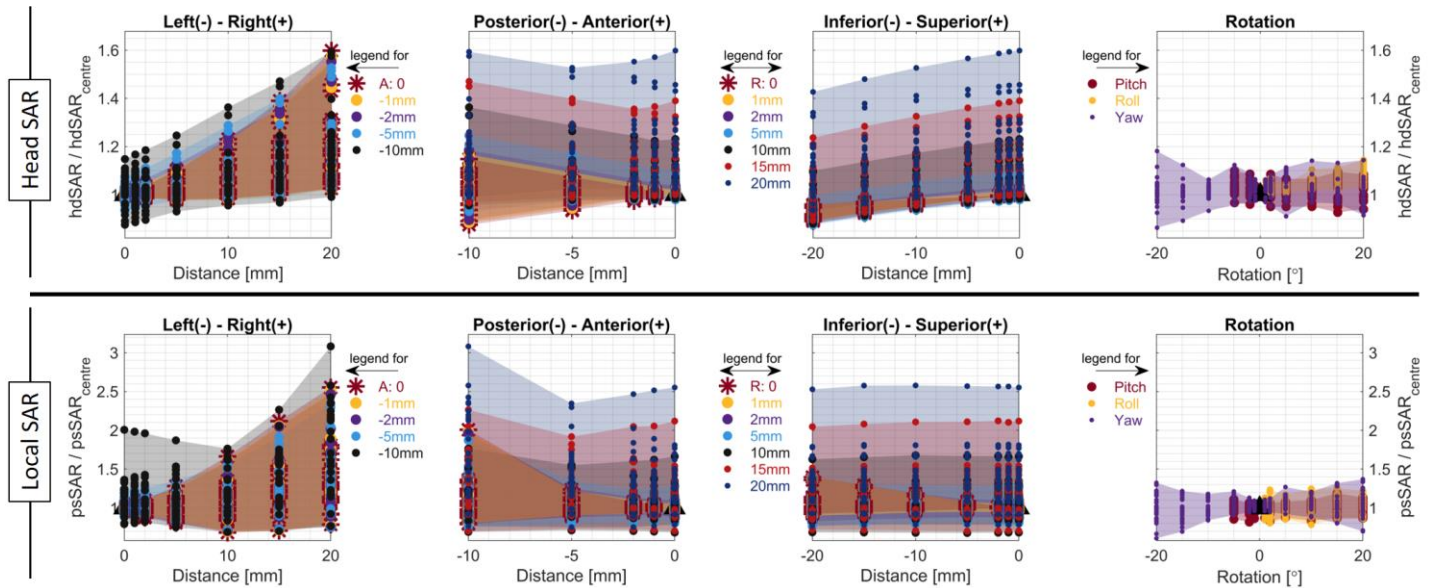
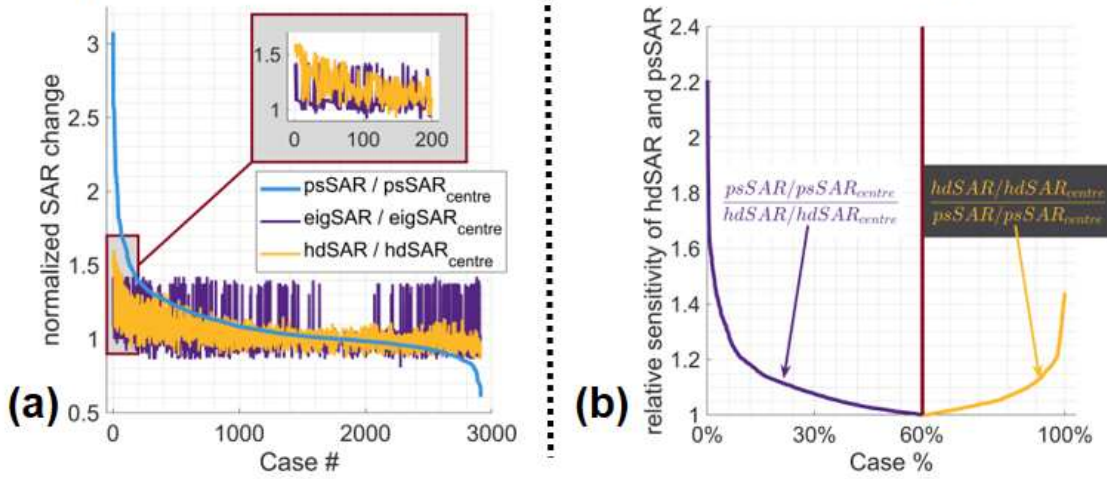


Figure 8: The variation of hdSAR and psSAR due to patient motion are compared for the 28 pTx pulses designed for the centred model. Whole-head SAR substantially underestimated the variation in peak local SAR, with the latter more than doubling for several cases. For any type and amount of motion, the area between the minimum and maximum SAR values across the 28 designed pulses were shaded in the same colour as the markers that identify the motion case (e.g., purple shading for R:10 mm, A:-2 mm cases in leftmost panels).



### pTx pulses designed for the centre, evaluated at each position



### All pulses designed for the centre, evaluated at each position

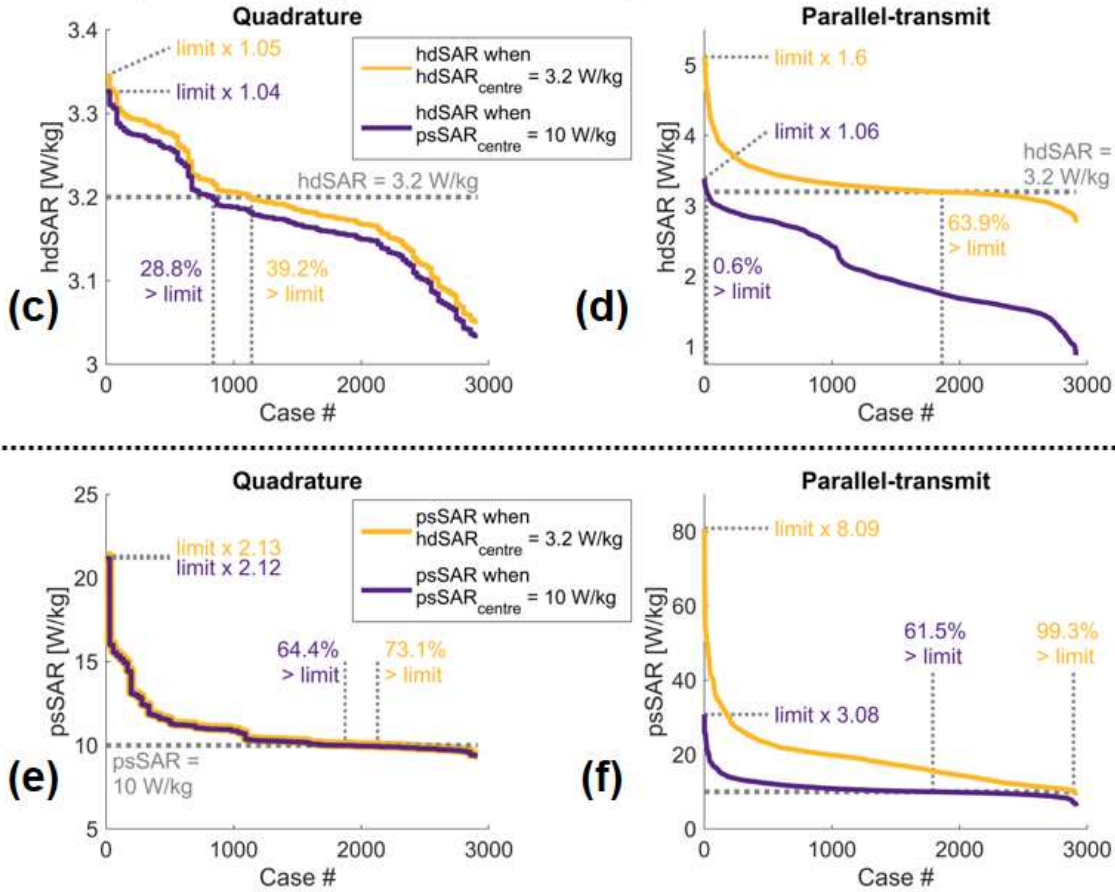


Figure 9: The variation of the SAR metrics due to motion for the pulses designed for the centre position are compared. (a) SAR metrics for the pTx pulses were normalized with their respective values at the centred position and sorted in decreasing order with respect to the change in psSAR. The maximum increases observed were; eigSAR, 42%; hdSAR, 60%; and psSAR, 210%. (b) In 60% of the cases investigated for pTx pulses, psSAR was up to 121% more sensitive to positional variations relative to hdSAR, and in 40% of the cases, hdSAR was up to 43% more sensitive relative to psSAR. (c-f) Panels compare how hdSAR and psSAR vary due to motion when either hdSAR or psSAR is used as the sole safety metric for quadrature (single-channel) and parallel-transmit pulses. Peak local SAR exceeded 10 W/kg in 62% of the cases when psSAR at the centre was set to 10 W/kg, and in almost all cases when hdSAR at the centre was set to 3.2 W/kg, for parallel-transmit.

## Pulses designed for each position, evaluated at their respective position

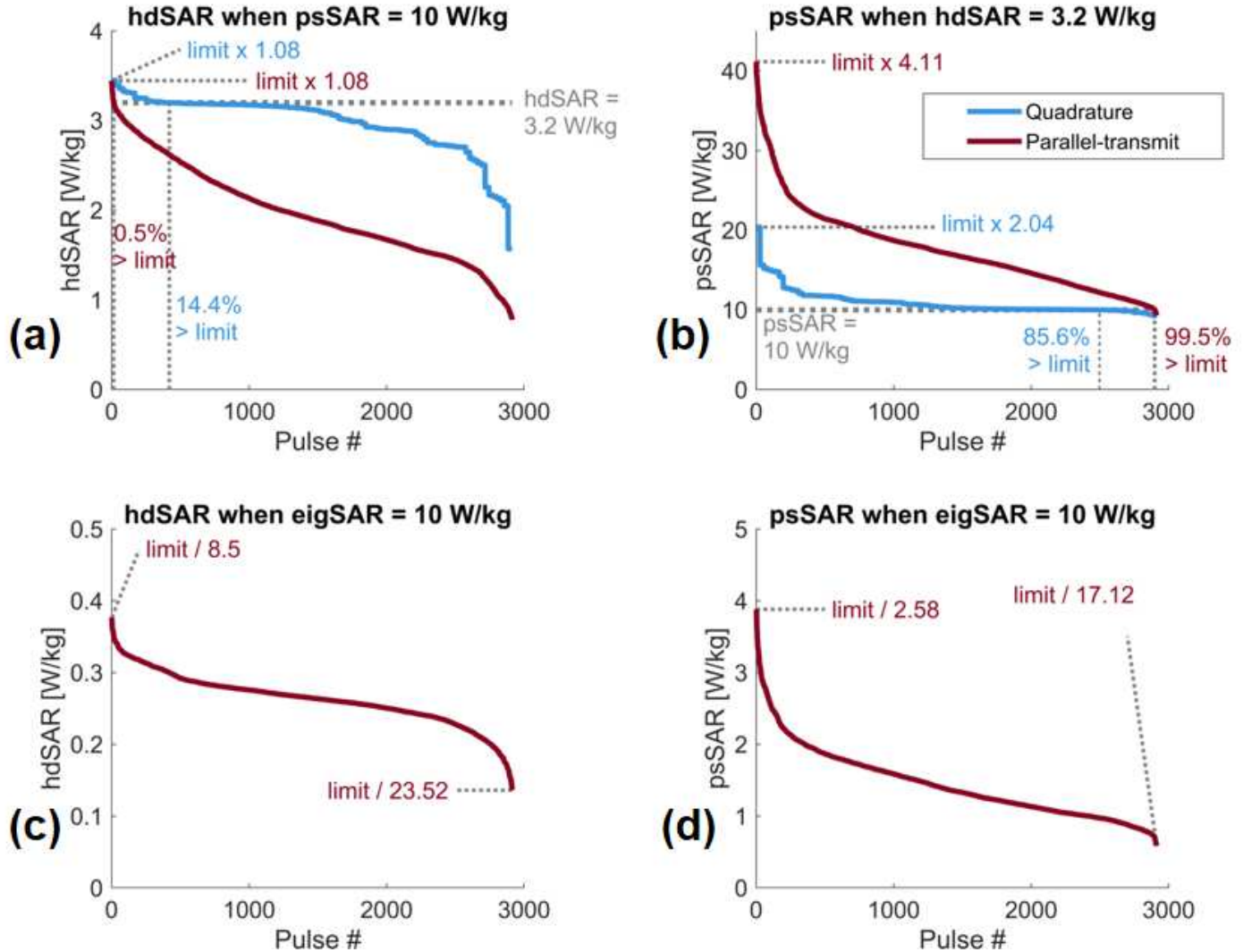
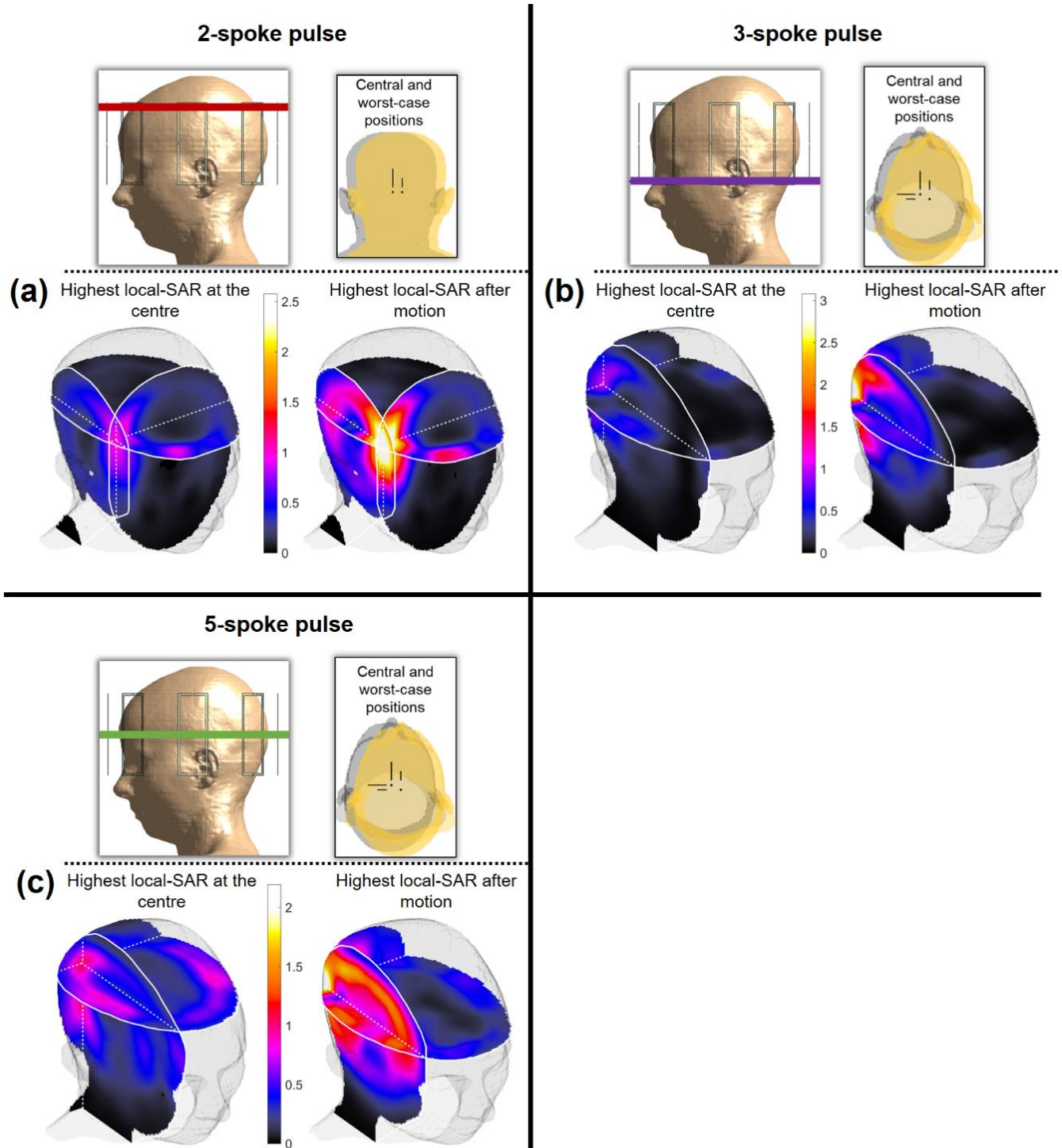


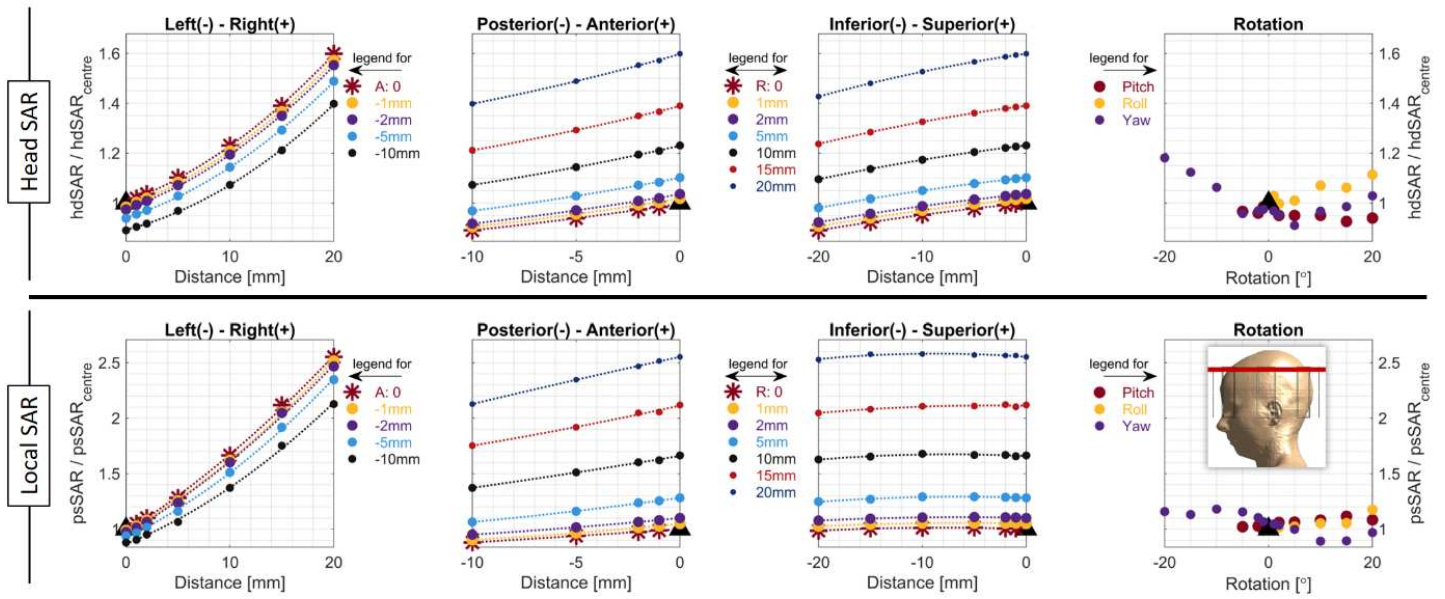
Figure 10: The SAR metrics eigSAR, psSAR and hdSAR are compared for all 5824 pulses (quadrature/parallel-transmit, 1-/2-/3-/5-spoke pulses, seven slices, 104 positions). For each pulse, sequence parameters were adjusted to yield (a) psSAR = 10 W/kg, (b) hdSAR = 3.2 W/kg, (c-d) eigSAR = 10 W/kg. When hdSAR was used as the sole safety metric and set to the limit (3.2 W/kg), peak local SAR values as high as 41 W/kg were observed (b). In a limited number of cases, using local SAR as the sole safety metric led to hdSAR exceeding the limit by up to 8% (a). EigSAR overestimated peak local SAR and whole-head SAR by at least 2.6-fold and 8.5-fold for parallel-transmit, respectively.

## SUPPORTING INFORMATION FIGURES

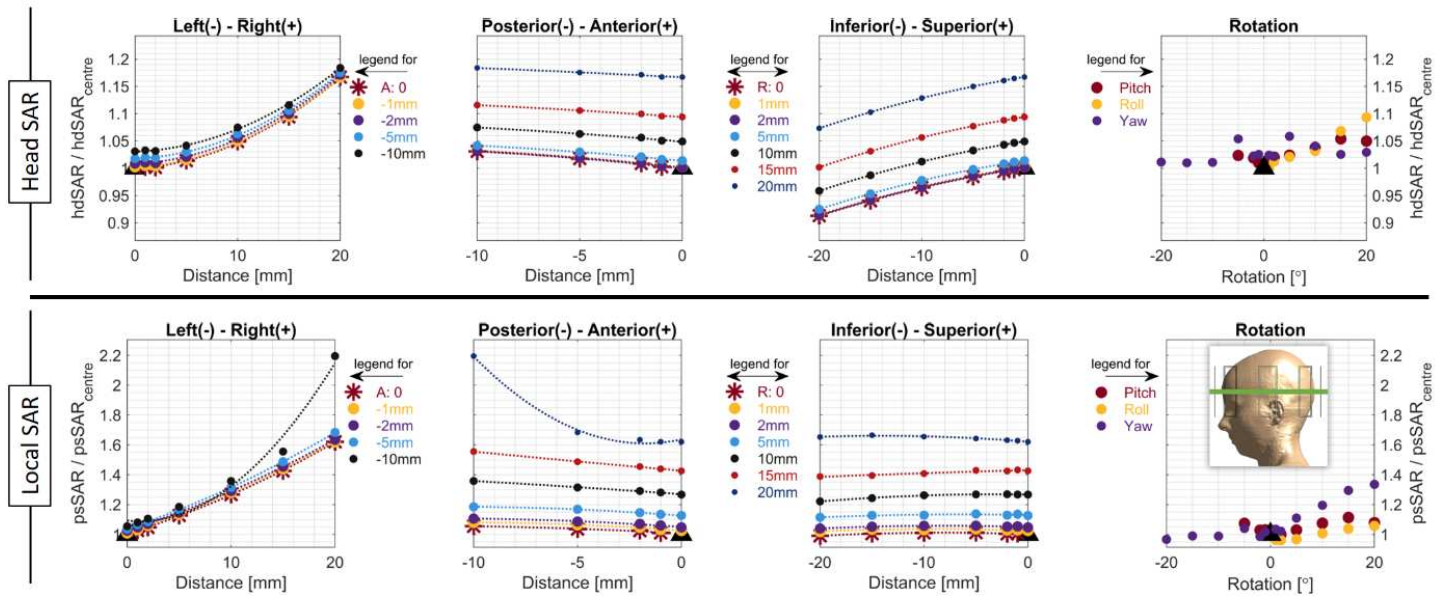


Supporting Information Figure S1: Three-dimensional comparisons show how local SAR changes with patient motion for three multi-spoke pulses. The worst-case increase was observed for R: 20 mm displacement for the 2-spoke pulse and R: 20 mm, P: 10 mm displacement for the 3-spoke and 5-spoke pulses. For the 2-spoke pulse, the local hotspot was in the right-anterior part of the brain whereas for the 3-spoke and 5-spoke pulses, it was in the right-posterior part. The location of the local hotspots did not change considerably for the three pulses shown here, although the peak local SAR increased **(a)** 2.6-fold for the 2-spoke pulse, **(b)** 3.1-fold for the 3-spoke pulse, and **(c)** 2.2-fold for the 5-spoke pulse.





Supporting Information Figure S2: The variation of whole-head and peak local SAR due to patient motion for a 2-spoke pulse (target slice shown on bottom right). Whole-head SAR (hdSAR) increased by up to 60%, whereas peak local SAR (psSAR) increased by up to 2.6-fold. Peak local SAR increased when the head moved towards right but decreased towards the posterior direction. In fact, the maximum increase in psSAR was not observed when the head was closest to the coils (R: 20 mm, A: -10 mm), but at R: 20 mm.



Supporting Information Figure S3: The variation of whole-head and peak local SAR due to patient motion for a 5-spoke pulse (target slice shown on bottom right). Whole-head SAR (hdSAR) increased by up to 18%, whereas peak local SAR (psSAR) increased by up to 2.2-fold.

## REFERENCES

1. Yacoub E, Shmuel A, Pfeuffer J, Van De Moortele PF, Adriany G, Andersen P, Vaughan JT, Merkle H, Ugurbil K, Hu X. Imaging brain function in humans at 7 Tesla. *Magn Reson Med* 2001;45(4):588-594.
2. Vaughan JT, Garwood M, Collins CM, Liu W, DelaBarre L, Adriany G, Andersen P, Merkle H, Goebel R, Smith MB, Ugurbil K. 7T vs. 4T: RF power, homogeneity, and signal-to-noise comparison in head images. *Magn Reson Med* 2001;46(1):24-30.
3. van der Kolk AG, Hendrikse J, Zwanenburg JJ, Visser F, Luijten PR. Clinical applications of 7 T MRI in the brain. *Eur J Radiol* 2013;82(5):708-718.
4. Malviya S, Voepel-Lewis T, Eldevik OP, Rockwell DT, Wong JH, Tait AR. Sedation and general anaesthesia in children undergoing MRI and CT: adverse events and outcomes. *Br J Anaesth* 2000;84(6):743-748.
5. Havidich JE, Beach M, Dierdorf SF, Onega T, Suresh G, Cravero JP. Preterm Versus Term Children: Analysis of Sedation/Anesthesia Adverse Events and Longitudinal Risk. *Pediatrics* 2016;137(3):e20150463.
6. Mallory MD, Travers C, McCracken CE, Hertzog J, Cravero JP. Upper Respiratory Infections and Airway Adverse Events in Pediatric Procedural Sedation. *Pediatrics* 2017;140(1).
7. Boriosi JP, Eickhoff JC, Klein KB, Hollman GA. A retrospective comparison of propofol alone to propofol in combination with dexmedetomidine for pediatric 3T MRI sedation. *Paediatr Anaesth* 2017;27(1):52-59.
8. Schwarz ST, Afzal M, Morgan PS, Bajaj N, Gowland PA, Auer DP. The 'swallow tail' appearance of the healthy nigrosome - a new accurate test of Parkinson's disease: a case-control and retrospective cross-sectional MRI study at 3T. *PLoS One* 2014;9(4):e93814.
9. Prasher V, Cumella S, Natarajan K, Rolfe E, Shah S, Haque MS. Magnetic resonance imaging, Down's syndrome and Alzheimer's disease: research and clinical implications. *J Intellect Disabil Res* 2003;47(Pt 2):90-100.
10. Greene DJ, Church JA, Dosenbach NUF, Nielsen AN, Adeyemo B, Nardos B, Petersen SE, Black KJ, Schlaggar BL. Multivariate pattern classification of pediatric Tourette syndrome using functional connectivity MRI. *Developmental Science* 2016;19(4):581-598.
11. Gemma M, Scola E, Baldoli C, Mucchetti M, Pontesilli S, De Vitis A, Falini A, Beretta L. Auditory functional magnetic resonance in awake (nonsedated) and propofol-sedated children. *Paediatr Anaesth* 2016;26(5):521-530.
12. Liu X, Lauer KK, Douglas Ward B, Roberts C, Liu S, Gollapudy S, Rohloff R, Gross W, Chen G, Xu Z, Binder JR, Li SJ, Hudetz AG. Propofol attenuates low-frequency fluctuations of resting-state fMRI BOLD signal in the anterior frontal cortex upon loss of consciousness. *Neuroimage* 2017;147:295-301.
13. Chen KT, Salcedo S, Chonde DB, Izquierdo-Garcia D, Levine MA, Price JC, Dickerson BC, Catana C. MR-assisted PET motion correction in simultaneous PET/MRI studies of dementia subjects. *Journal of magnetic resonance imaging : JMIR* 2018;48(5):1288-1296.
14. Kecskemeti S, Samsonov A, Velikina J, Field AS, Turski P, Rowley H, Lainhart JE, Alexander AL. Robust Motion Correction Strategy for Structural MRI in Unsedated Children Demonstrated with Three-dimensional Radial MPnRAGE. *Radiology* 2018;289(2):509-516.
15. Kraff O, Fischer A, Nagel AM, Monninghoff C, Ladd ME. MRI at 7 Tesla and above: demonstrated and potential capabilities. *J Magn Reson Imaging* 2015;41(1):13-33.
16. Fiedler TM, Ladd ME, Bitz AK. SAR Simulations & Safety. *NeuroImage* 2018;168:33-58.
17. Ugurbil K, Xu J, Auerbach EJ, Moeller S, Vu AT, Duarte-Carvajalino JM, Lenglet C, Wu X, Schmitter S, Van de Moortele PF, Strupp J, Sapiro G, De Martino F, Wang D, Harel N, Garwood M, Chen L, Feinberg DA, Smith SM, Miller KL, Sotiropoulos SN, Jbabdi S, Andersson JL, Behrens TE, Glasser MF, Van Essen DC, Yacoub E, Consortium WU-MH. Pushing spatial and temporal resolution for functional and diffusion MRI in the Human Connectome Project. *Neuroimage* 2013;80(0):80-104.
18. Ugurbil K. Imaging at ultrahigh magnetic fields: History, challenges, and solutions. *NeuroImage* 2017.
19. Setsompop K, Kimmlingen R, Eberlein E, Witzel T, Cohen-Adad J, McNab JA, Keil B, Tisdall MD, Hoecht P, Dietz P, Cauley SF, Tountcheva V, Matschl V, Lenz VH, Heberlein K, Potthast A, Thein H, Van Horn J, Toga A, Schmitt F, Lehne D, Rosen BR, Wedeen V, Wald LL. Pushing the limits of in vivo diffusion MRI for the Human Connectome Project. *Neuroimage* 2013;80:220-233.
20. Padormo F, Beqiri A, Hajnal JV, Malik SJ. Parallel transmission for ultrahigh-field imaging. *NMR Biomed* 2016;29(9):1145-1161.
21. Seifert F, Wübbeler G, Junge S, Ittermann B, Rinneberg H. Patient safety concept for multichannel transmit coils. *Journal of Magnetic Resonance Imaging* 2007;26(5):1315-1321.
22. Wang Z, Lin JC, Mao W, Liu W, Smith MB, Collins CM. SAR and temperature: Simulations and comparison to regulatory limits for MRI. *Journal of Magnetic Resonance Imaging* 2007;26(2):437-441.
23. Massire A, Cloos MA, Luong M, Amadon A, Vignaud A, Wiggins CJ, Boulant N. Thermal simulations in the human head for high field MRI using parallel transmission. *J Magn Reson Imaging* 2012;35(6):1312-1321.
24. de Greef M, Ipek O, Raaijmakers AJ, Crezee J, van den Berg CA. Specific absorption rate intersubject variability in 7T parallel transmit MRI of the head. *Magn Reson Med* 2013;69(5):1476-1485.
25. Brunner DO, Pruessmann KP. Optimal design of multiple-channel RF pulses under strict power and SAR constraints. *Magn Reson Med* 2010;63(5):1280-1291.
26. Guerin B, Gebhardt M, Cauley S, Adalsteinsson E, Wald LL. Local specific absorption rate (SAR), global SAR, transmitter power, and excitation accuracy trade-offs in low flip-angle parallel transmit pulse design. *Magn Reson Med* 2014;71(4):1446-1457.
27. Deniz CM, Alon L, Brown R, Zhu Y. Subject- and resource-specific monitoring and proactive management of parallel radiofrequency transmission. *Magn Reson Med* 2016;76(1):20-31.
28. Boulant N, Massire A, Amadon A, Vignaud A. Radiofrequency pulse design in parallel transmission under strict temperature constraints. *Magn Reson Med* 2014;72(3):679-688.
29. Lee J, Gebhardt M, Wald LL, Adalsteinsson E. Local SAR in parallel transmission pulse design. *Magn Reson Med* 2012;67(6):1566-1578.
30. Christ A, Kainz W, Hahn EG, Honegger K, Zefferer M, Neufeld E, Rascher W, Janka R, Bautz W, Chen J, Kiefer B, Schmitt P, Hollenbach H-P, Shen J, Oberle M, Szczerba D, Kam A, Guag JW, Kuster N. The Virtual Family—development of surface-based anatomical models of two adults and two children for dosimetric simulations. *Physics in Medicine & Biology* 2010;55(2):N23.

31. Makris N, Angelone L, Tulloch S, Sorg S, Kaiser J, Kennedy D, Bonmassar G. MRI-based anatomical model of the human head for specific absorption rate mapping. *Medical & Biological Engineering & Computing* 2008;46(12):1239-1251.
32. Visible Human Project. U.S. National Library of Medicine.
33. Bardati F, Borrani A, Gerardino A, Lovisolo GA. SAR optimization in a phased array radiofrequency hyperthermia system. *IEEE Transactions on Biomedical Engineering* 1995;42(12):1201-1207.
34. Graesslin I, Homann H, Biederer S, Börner P, Nehrke K, Vernickel P, Mens G, Harvey P, Katscher U. A specific absorption rate prediction concept for parallel transmission MR. *Magn Reson Med* 2012;68(5):1664-1674.
35. Eichfelder G, Gebhardt M. Local specific absorption rate control for parallel transmission by virtual observation points. *Magn Reson Med* 2011;66(5):1468-1476.
36. Gumbrecht R, Fontius U, Adolf H, Benner T, Schmitt F, Adalsteinsson E, Wald L, Fautz H. Online local SAR supervision for transmit arrays at 7T. 2013. p 4420.
37. Ipek O, Raaijmakers AJ, Lagendijk JJ, Luijten PR, van den Berg CA. Intersubject local SAR variation for 7T prostate MR imaging with an eight-channel single-side adapted dipole antenna array. *Magn Reson Med* 2014;71(4):1559-1567.
38. International Electrotechnical Commission. Medical electrical equipment-Part 2-33: Particular requirements for the basic safety and essential performance of magnetic resonance equipment for medical diagnosis. IEC 60601-2-33 Ed 32. 2015.
39. United States Food and Drug Administration. Guidance for Industry and Food and Drug Administration Staff – Criteria for Significant Risk Investigations of Magnetic Resonance Diagnostic Devices. 2014.
40. Ferrand G, Luong M, Amadon A, Boulant N. Mathematical tools to define SAR margins for phased array coil in-vivo applications given E-field uncertainties. 2015. p 1862.
41. Le Garrec M, Gras V, Hang MF, Ferrand G, Luong M, Boulant N. Probabilistic analysis of the specific absorption rate intersubject variability safety factor in parallel transmission MRI. *Magn Reson Med* 2017;78(3):1217-1223.
42. Boulant N, Gras V, Amadon A, Luong M, Ferrand G, Vignaud A. Workflow proposal for defining SAR safety margins in parallel transmission. 2018.
43. Gras V, Vignaud A, Amadon A, Bihan D, Boulant N. Universal pulses: A new concept for calibration-free parallel transmission. *Magn Reson Med* 2017;77(2):635-643.
44. Wolf S, Diehl D, Gebhardt M, Mallow J, Speck O. SAR simulations for high-field MRI: how much detail, effort, and accuracy is needed? *Magn Reson Med* 2013;69(4):1157-1168.
45. Shajan G, Kozlov M, Hoffmann J, Turner R, Scheffler K, Pohmann R. A 16-channel dual-row transmit array in combination with a 31-element receive array for human brain imaging at 9.4 T. *Magn Reson Med* 2014;71(2):870-879.
46. Shao Y, Zeng P, Wang S. Statistical simulation of SAR variability with geometric and tissue property changes by using the unscented transform. *Magn Reson Med* 2015;73(6):2357-2362.
47. Murbach M, Neufeld E, Kainz W, Pruessmann KP, Kuster N. Whole-body and local RF absorption in human models as a function of anatomy and position within 1.5T MR body coil. *Magn Reson Med* 2014;71(2):839-845.
48. Murbach M, Cabot E, Neufeld E, Gosselin M-C, Christ A, Pruessmann KP, Kuster N. Local SAR enhancements in anatomically correct children and adult models as a function of position within 1.5 T MR body coil. *Progress in Biophysics and Molecular Biology* 2011;107(3):428-433.
49. Murbach M, Neufeld E, Cabot E, Zastrow E, Corcoles J, Kainz W, Kuster N. Virtual population-based assessment of the impact of 3 Tesla radiofrequency shimming and thermoregulation on safety and B1 + uniformity. *Magn Reson Med* 2016;76(3):986-997.
50. Murbach M, Neufeld E, Samaras T, Corcoles J, Robb FJ, Kainz W, Kuster N. Pregnant women models analyzed for RF exposure and temperature increase in 3T RF shimmed birdcages. *Magn Reson Med* 2017;77(5):2048-2056.
51. Deniz CM, Vaidya MV, Sodickson DK, Lattanzi R. Radiofrequency energy deposition and radiofrequency power requirements in parallel transmission with increasing distance from the coil to the sample. *Magn Reson Med* 2016;75(1):423-432.
52. Katscher U, Röhrs J, Börner P. Basic considerations on the impact of the coil array on the performance of Transmit SENSE. *Magn Reson Mater Phy* 2005;18(2):81-88.
53. IEC/IEEE International Standard -- Determining the peak spatial-average specific absorption rate (SAR) in the human body from wireless communications devices, 30 MHz to 6 GHz - Part 1: General requirements for using the finite-difference time-domain (FDTD) method for SAR calculations. IEC/IEEE 62704-1:2017 2017:1-86.
54. Kopanoglu E, Constable RT. Radiofrequency pulse design using nonlinear gradient magnetic fields. *Magn Reson Med* 2015;74(3):826-839.
55. Grissom WA, Setsompop K, Hurley SA, Tsao J, Velikina JV, Samsonov AA. Advancing RF pulse design using an open-competition format: Report from the 2015 ISMRM challenge. *Magn Reson Med* 2017;78(4):1352-1361.
56. Grissom W, Yip CY, Zhang Z, Stenger VA, Fessler JA, Noll DC. Spatial domain method for the design of RF pulses in multicoil parallel excitation. *Magn Reson Med* 2006;56(3):620-629.
57. Hestenes MR, Stiefel E. Methods of Conjugate Gradients for Solving Linear Systems. *Journal of Research of the National Bureau of Standards* 1952;49(6):409-436.
58. Mallat SG, Zhang ZF. Matching Pursuits with Time-Frequency Dictionaries. *IEEE Transactions on Signal Processing* 1993;41(12):3397-3415.
59. Grissom WA, Khalighi MM, Sacolick LI, Rutt BK, Vogel MW. Small-tip-angle spokes pulse design using interleaved greedy and local optimization methods. *Magn Reson Med* 2012;68(5):1553-1562.
60. Kopanoglu E. Near real-time parallel-transmit pulse design. *Proc. ISMRM and ESMRMB*; 2018; Paris, France. p 3392. (Proc. ISMRM and ESMRMB).
61. Lustig M, Kim SJ, Pauly JM. A fast method for designing time-optimal gradient waveforms for arbitrary k-space trajectories. *IEEE Trans Med Imaging* 2008;27(6):866-873.
62. Pauly J, Le Roux P, Nishimura D, Macovski A. Parameter relations for the Shinnar-Le Roux selective excitation pulse design algorithm [NMR imaging]. *IEEE Trans Med Imaging* 1991;10(1):53-65.
63. Conolly S, Nishimura D, Macovski A, Glover G. Variable-Rate Selective Excitation. *Journal of Magnetic Resonance* 1988;78(3):440-458.
64. International Electrotechnical C. Medical electrical equipment-Part 2-33 : Particular requirements for the basic safety and essential performance of magnetic resonance equipment for medical diagnosis. IEC 60601-2-33 Ed 30 2010.